IET Optoelectronics

Special Issue Call for Papers

Be Seen. Be Cited. Submit your work to a new IET special issue

Connect with researchers and experts in your field and share knowledge.

Be part of the latest research trends, faster.

Read more

IET Optoelectronics

ORIGINAL RESEARCH

Carrier synchronisation in multiband carrierless amplitude and phase modulation for visible light communication-based IoT systems

Luís Rodrigues[1,2] 🅾 | Mónica Figueiredo[2,3] 🅾 | Luís Nero Alves[1,2] | Zabih Ghassemlooy[4]

[1]Department of Electronics, Telecommunications and Informatics, University of Aveiro, Aveiro, Portugal

[2]Instituto de Telecomunicações, Aveiro, Portugal

[3]School of Technology and Management, Polytechnic of Leiria, Leiria, Portugal

[4]Optical Communications Research Group, Faculty of Engineering and Environment, Northumbria University, Newcastle upon Tyne, UK

Correspondence

Luís Rodrigues, Department of Electronics, Telecommunications and Informatics, University of Aveiro, Aveiro 3810-193, Portugal.
Email: luis.abade@ua.pt

Abstract

The technical feasibility of developing an Internet of Things multi-user communication system is evaluated based on a central digital multiband carrierless amplitude and phase transmitter, which broadcasts data on multiple channels for a number of low-cost/low-power devices. It addresses the issue of carrier synchronisation, which is critical in real-world implementations because of imperfections of devices and the delays of the system. A simulation model for the traditional Costas Loop is presented, along with performance results, which demonstrate the system's ability to synchronise with pull-in and lock ranges of ±800 and ±900 Hz, respectively. The loop requires 1.194 ms to be in the locked state, allowing the system to lock within 6 symbols period. In addition, the authors measured the performance of the system in the presence of noise and interference from other modulated bands. The results showed that noise and interference did not degrade the system's performance. Although the system was unable to lock when energy was present in adjacent bands, alternative options such as a high order phase-locked loop and hybrid frequency-division multiple access and time-division multiple access, can improve system performance without significantly increasing the cost and complexity of the devices.

KEYWORDS

demodulation, frequency division multiple access, indoor communication, synchronisation

1 | INTRODUCTION

Over the years, the paradigm of common electronic gadgets has been shifting. Various household appliances, wearable technology, and entertainment systems are now gradually integrating wireless communication capabilities [1] and becoming connected to the Internet, enabling cooperation between them [2]. According to Cisco, 14.7 billion of the internet-connected devices will be machine-to-machine connections by the end of 2023, corresponding to half of all Internet connections [3]. However, as the number of devices increases, it will become more challenging to maintain current technologies, since these devices will have smaller sizes, low cost, and consume less power [4, 5]. Currently, wireless IoT systems primarily use radio-frequency (RF) technology, such as Bluetooth, ZigBee, LoRaWAN, and NB-IoT [1]. However, in high-density device scenarios, the limited availability of spectrum can cause performance issues [6]. Further, these technologies often use industrial, scientific, and medical (ISM) bands [7] and may require commercial licensing, which increase the cost of large networks of wireless devices.

Visible light communication (VLC) may be a suitable alternative technology to RF systems as it enables spectrum reuse within a short distance. VLC is achieved by the intensity modulation of a light source, typically a light emitting diode LED due to its reasonable modulation bandwidth, driving simplicity, low cost, and illuminating functionality. Compared to RF, light rays are highly directional, which allows for easy reuse of the available spectrum while also offering other benefits such as embedded communication in lighting systems [8]. Adopting VLC into IoT scenarios may alleviate some of the limitations caused by current RF technologies. In fact,

optical wireless communications (OWC), which includes VLC, is currently considered for short-range and indoor IoT scenarios [1].

In recent years, we have witnessed a growing interest in the use of VLC for a variety of purposes. In 2018, VLC demonstrator of a mobile robot in a production line was presented, achieving more than 100 Mbit/s and 5 ms latency communication [9]. VLC smart labels have also been proposed as an interesting application, as many devices can be updated simultaneously using the existing lighting system, rather than RF identification or infrared communications [10, 11]. In Ref. [12], IoT RF devices can potentially improve security by using VLC to configure the device during initialisation rather than using an unsecure RF channel. Others have proposed VLC-based IoT devices with residual power consumption by reflecting a modulated version of an external light source. Thus, eliminating the need for the devices to have their own light source, one of the most power demanding components of VLC-based IoT devices, and reducing the device's power consumption [13–17]. These proposals fail to address both the IoT device requirements (low power, low cost, and small size) and system multi-user requirements in scenarios with high IoT device density. While most of the systems target single devices, multiple-user architectures are usually based in complex modulation schemes such as orthogonal frequency-division multiple access or code division multiple access which require high processing capabilities, thus increasing the cost and power consumption of the receiver (Rx) devices. Multiple-user capability was addressed in Ref. [18] by proposing the usage of multiband carrierless amplitude and phase (m-CAP) modulation as a frequency-domain multiple access scheme, however a real implementation of the Rx would require digital receivers with high capability digital signal processors (DSPs), leading to high cost and power consumption devices. In Ref. [19], it was proposed that the m-CAP modulation could accommodate multiple user scenarios without ignoring the cost of implementing digital receivers in IoT devices. The proposed system considered a low cost and low power broadcast architecture with digital modulation for all the users, and analogue-based homodyne Rx. This was followed by experimental investigation of a multiple-user architecture using m-CAP with analogue Rxs [20]. Such analogue devices can be easily implemented in an integrated circuit with less transistors than the digital equivalent, effectively decreasing its cost and power consumption.

In coherent systems there is the need for synchronisation between the carrier signal at the Tx and at the Rx to ensure successful demodulation and decoding of the information. This is best achieved by synchronising both the frequency and phase of the carrier signal at the Rx, which can be done using a phase-locked loop (PLL). For complex modulations, such as quadrature amplitude modulation (QAM) and CAP, a simple PLL is not sufficient since the carrier is implicit in the modulated signal, that is, the phase of the signal is not constant makes it impossible to acquire the lock state with a PLL. Since the carrier signal is suppressed in these modulations, that is, no energy allocated to the carrier, it is necessary to revert the

effects in order to recover the carrier signal. Costas-loop is a synchronisation loop commonly used for suppressed carrier modulations [21]. This paper presents the use of a Costas-loop to recover the central frequency of a m-CAP band, thus the need for mitigating both frequency and phase offsets in a VLC-based IoT system which uses multiple analogue Rxs [20, 22]. While synchronisation circuits should be built with low hardware resources to cope with the IoT requirements, a trade-off between complexity and performance must be considered. The limitation is primarily related to the tolerance and stability of electronic components, mainly the crystal oscillators widely used in low cost and high precision frequency devices. In this paper, a type-II loop is implemented, allowing frequency recovery without phase offset when a step in frequency occurs. Due to their relative slowness compared to the carrier frequency to be recovered, temperature induced and Doppler frequency shift are not considered.

The main contributions of this paper are:

- Validate the usage of a Costas-loop with m-CAP modulation;
- Estimate the number of symbols to perform carrier synchronisation in the preamble of the physical layer frame;
- Analysis of the viability analysis of a real-world implementation of Costas-loop in VLC-based IoT systems due to impairments of the oscillators.

The paper is structured as follows. Section 1 provides the necessary background of VLC systems and presents the motivation behind VLC-based IoT systems. Section 2 presents the theoretical background of a hybrid CAP/QAM system that can be used in the targeted application, with an extended overview of the carrier synchronisation. Sections 3 and 4 explain the simulation setup and the respective results of the carrier synchroniser. The paper conclusions are presented in the last section.

2 | SYSTEM ARCHITECTURE

A typical single-input multiple-output (SIMO) VLC-based system is shown in Figure 1, where the data received from the Internet is transmitted to the devices via the light. In accordance with the bandwidth requirements of each device, the frequency spectrum is divided to allocate a set of frequencies to each device, see Figure 2. Considering such scenarios, it is expected a high number of Rx devices, the frontend optimisation regarding low-cost is more profitable if done in the Rx side. In the same scenarios, the Rx device does usually have low-power requirements, since they are battery powered devices. In this work the aim is to optimise the Rx frontend in order to fulfil the requirements of low-power and low-cost of Rx devices in VLC-based SIMO architecture.

The system architecture is presented in Figure 3. The input data stream is modulated with m-CAP modulation using high-speed DSPs, and then converted into an analogue voltage prior to intensity modulation of the light source via the driver unit.

At the receiver side, combination of a photodiode (PD) and a transimpedance amplifier are used to regenerate the electrical signal. The analogue demodulator performs the data symbols' recovery, with a PLL to ensure synchronisation of the carrier. In fact, since m-CAP is a type of a carrier suppressed modulation format, a Costas-loop can be used, which will be discussed in details in Section 2.3. A comparator is used to regenerate the data stream. Note some degree of hysteresis is included to eliminate multiple transmissions caused by noise. The regenerated digital stream is then oversampled using a simple and low cost micro controller (μC) for extracting the data bits.
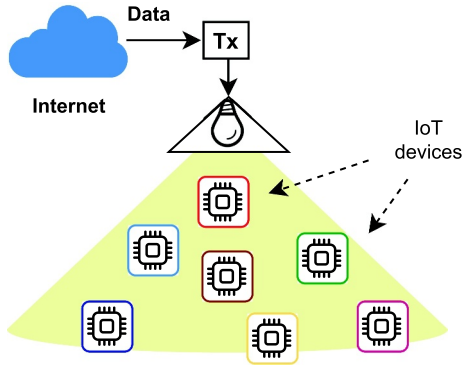

FIGURE 1 Example of a SIMO VLC-based system—one Tx broadcasts to many IoT devices. SIMO, single-input multiple-output; VLC, visible light communication.
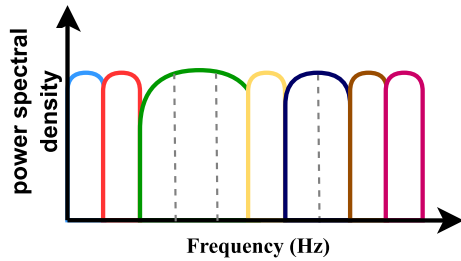

FIGURE 2 VLC bands distribution for the IoT devices. Each device operates in a different set of frequencies, here represented by different colours. VLC, visible light communication.
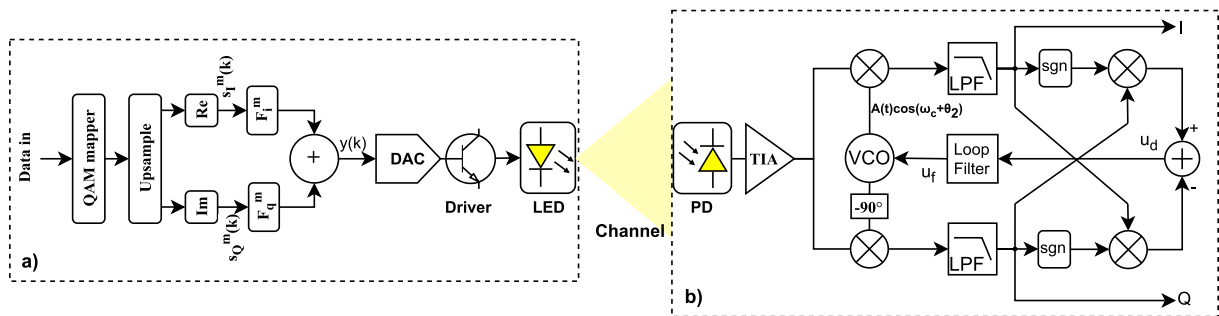
2.1 | The transmitter

The Tx block diagram is shown in Figure 3a. It features a conventional m-CAP design with digital finite impulse response filters that upsample and filter pulse amplitude modulation signals as inputs. The combined signal is given as:

$$y(k) = \sqrt{2} \sum_{m=1}^{M} \left(s_I^m(k) * F_I^m(k) - s_Q^m(k) * F_Q^m(k) \right), \quad (1)$$

where k is the sample index, M is the total number of bands, s_I and s_Q are the data symbols, F_I^m and F_Q^m are the in-phase I, and quadrature Q filters, respectively. The filters' coefficients are given by Equations (2) and (3), where $p(k)$ is a pulse shaping filter and $\omega_c^m = 2\pi f_c^m$, f_c^m is the central frequency on the mth band, and F_s is the sampling frequency.

$$F_I^m(k) = p(k)\cos\left(\frac{\omega_c^m}{F_s}k\right), \quad (2)$$

$$F_Q^m(k) = p(k)\sin\left(\frac{\omega_c^m}{F_s}k\right). \quad (3)$$

Each band's central frequency $f_c^m = B(2m-1)/2$, where B is the bandwidth. In m-CAP systems, Nyquist filters are commonly used to ensure minimal intersymbol interference (ISI), but are difficult to implement in the analogue domain. When the Rx filter is matched with the Tx filter, some ISI can be allowed, and alternative filters may be employed for $p(k)$. Bessel filters were found to be the most suitable for analogue m-CAP demodulation in Ref. [19], which studied the selection of $p(k)$ for hybrid m-CAP/QAM.

Following conversion of $y(k)$ into an analogue signal using a digital-to-analogue converter, it is used as a current driver module for intensity modulation of the LED. The Tx parameters are summarised in the Table 1.

2.2 | The receiver

At the Rx side, the optical signal is converted to an electrical signal using a PD and a TIA prior to being demodulated using

FIGURE 3 Hybrid CAP/QAM VLC system architecture for IoT using digital m-CAP modulator and analogue receivers: (a) the Tx block diagram for the mth band, and (b) the Rx block diagram, including carrier synchronisation (Costas-loop). CAP, carrierless amplitude and phase; QAM, quadrature ampliture modulation; VLC, visible light communication.

TABLE 1 System parameters.

Parameter	Value
Number of bands (m)	100
Data rate per band	10 kbit/s
Bits/symbol	2 bits/symbol
Symbol rate (R)	5 kHz
Carrier frequency (f_c)	25 kHz
Bessel filter order	8
Band bandwidth (B)	10 kHz

a homodyne Rx as shown in Figure 3b. Note, the low-pass filters (LPF) are Bessel filters, and a Costas Loop PLL is used to ensure that the VCO is running at the exact the carrier frequency f_c. The following section explains its operating principle in higher detail. Note, the Rx generated carrier is a square-wave since it can be implemented at a lower cost, which shown to have identical performance when compared to a sine-wave in Ref. [23].

2.3 | The carrier synchronisation—The Costas-loop

The Costas-loop is a variation of a PLL that is suitable to perform carrier synchronisation in suppressed carrier modulations. The loop operates at two different states: unlock and lock. The simplified operating principle can be understood as follows. The symbols are demodulated by multiplying the received signal with a reference frequency with some offset with reference to the transmitted carrier wave. As a result, the constellation rotates continuously, due to the increasing phase difference between signals. Note that the control signal to the VCO remains constant provided both signals are in perfect sync. However, small changes to the signal at the Tx or the Rx will result in the rotation of the constellation. The Costas-loop error detector defines four stable states for the loop, that is, a stable signal at the VCO input, correspondent to the constellation depicted in Figure 4. Due to a difference in the carrier and the VCO output, the loop will act with an opposite reaction to counteract the rotation of the constellation. This is known as pull-in, which occurs when the Costas-loop is in the lock state, continuously adjusting the local oscillator frequency f_{LO} to match the f_c. Note, a capture range Δf_P is defined as the, frequency range between f_c and f_{LO} while in the lock state is known as capture range. During the unlocked state, the Costas-loop adjusts the output frequency until it enters the lock state, which has a wider frequency range, referred to as the lock range Δf_L. The frequency ranges are shown in Figure 5. Acquisitions and pull-in processes require different times to complete, while the pull-in time T_P being much shorter than acquisition time T_L.

Figure 6 depict the three blocks of a PLL, which can also be applied to the PLL Costas-loop: phase detector (PsD), loop-filter (LF), and VCO. In general, PLLs and Costas-loops
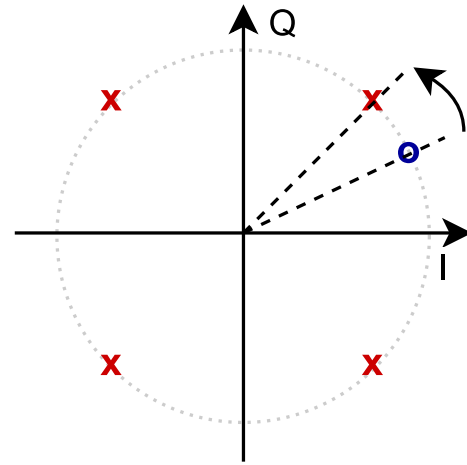

FIGURE 4 Quadrature amplitude modulation constellation: the red 'x' marks represent the reference constellation and the blue 'o' mark represents an Rx symbol with a phase difference between f_c and f_{LO}. The Costas-loop action will result in a constellation rotation to match the Rx symbols with the reference constellation.
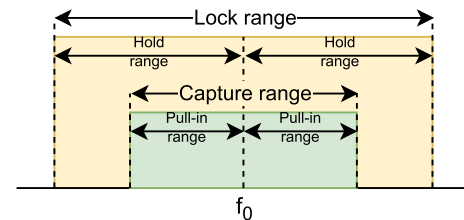

FIGURE 5 Frequency ranges used to characterise phase-locked loops: lock range and capture range which can be subdivided in hold range and pull-in range, respectively.
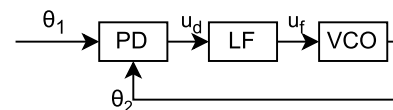

FIGURE 6 Costas-loop model: PsD, LF, and VCO. LF, loop filter; PsD, phase detector; VCO, voltage-controlled oscillator.

can be categorised based on their order and type, where the former refer to the number of poles in the loop transfer function, while the later is the number of integrators. In addition to increasing the noise rejection ratio, increasing the order of the loop makes it more difficult to stabilise the loop due to the phase margin. However, the type of a PLL indicates how much accurate the phase is when a frequency offset occurs, which also improves the performance for higher loop types, at the cost of stability margins. Note, a type-I loops will always exhibit a static phase error when the frequency is changed by a step, whereas a type-II loop will eliminate the phase error in this situation. However, when the frequency change linear (i.e. a ramp), the type-II loop is not able to eliminate phase, resulting in the need for a type-III loop.

The PsD compares both input and generated wave phases θ_1 and θ_2, respectively, resulting in a phase error $\theta_e = \theta_1 - \theta_2$.

The PsD output signal is a voltage u_d, which is proportional to θ_e, and, in case of QAM, if θ_e is relatively small, that is, the loop is in locked state, which can be approximated by:

$$u_d(t) = 2A(t)\ \theta_e(t) = K_d\theta_e(t), \tag{4}$$

where A is the modulation amplitude of each I and Q branch, and K_d is the PsD gain. As shown in Figure 3b, u_d is obtained by multiplication processes, resulting in high frequency components at $2w_c$ that must be properly filtered Using a first order LPF with a transfer function of:

$$H_{LPF}(s) = \frac{1}{1 + s/\omega_3} \tag{5}$$

where ω_3 is the cut-off frequency. Hence, from Equations (4) and (5) the transfer function of PsD is given as:

$$H_{PsD}(s) = \frac{U_d(s)}{\Theta_e(s)} = \frac{K_d}{1 + s/\omega_3} \tag{6}$$

Following in the loop chain, the LF will filter out noise and any other high frequency components, allowing the loop to stabilise at the locked state. The LF can be implemented according to the desired behaviour of the Costas-loop. Generally, lag (one pole), lag–lead filters (pole-zero pair), and PI (proportional + integral) filters may be used to implement the LF. A type-II loop is obtained by selecting a PI filter, whose transfer function is given by:

$$H_{LF}(s) = \frac{U_f(s)}{U_d(s)} = \frac{1 + s\tau_2}{s\tau_1} \tag{7}$$

where τ_1 and τ_2 are the time constants of the filter, and $\omega_{LP} = 1/\tau_2$ is the angular frequency of the filter zero.

The signal $u_f(t)$ directly controls the VCO, that converts the input voltage signal into a frequency. The VCO has a quiescent frequency $f_{\text{quiescient}}$, that is, the output frequency $f_{LO} = f_{\text{quiescient}} + u_f K_0$, where K_0 is the VCO gain. Real-world VCOs are typically implemented with a voltage controlled crystal oscillator, where the crystal is used as the frequency reference. Hence, the impairments of the crystal oscillator are crucial, namely the accuracy of the frequency [24]. Typical crystal oscillators have an accuracy of about ± 100 ppm, which for a maximum $f_c \approx 1 \times 10^6$ Hz, it corresponds to a 100 Hz frequency offset. In the worst case, when the offsets between the Tx and the Rx are opposite each other, the total frequency offset $\Delta f_{\text{total}} = \pm 200$ Hz. The general VCO transfer function is given by:

$$H_{VCO}(s) = \frac{\Theta_2(s)}{U_f(s)} = \frac{K_0}{s} \tag{8}$$

The open loop transfer function is given by Equation (9). The loop has three poles and two integrators, therefore it is a third-order and type-II loop.

$$G_{OL}(s) = \frac{K_d}{1 + s/\omega_3} \frac{1 + s\tau_1}{s\tau_2} \frac{K_0}{s} \tag{9}$$

Note, for the loop to be stable, the phase margin must be $>45°$ when $G_{OL} > 1$. Therefore, the loop parameters (ω_3, ω_{LP}, τ_1 and K_0) must be computed so that the high frequency noises are eliminated while maintaining the loop stability [25].

3 | SIMULATION SETUP

We have developed a MatLab® Simulink® model of m-CAP modulation for VLC-based IoT applications, including a carrier synchroniser implemented by the Costas-loop for QAM, see Figure 7. In the Tx side, the outputs of random number generators (rngs) are applied to m-CAP modulators with f_c of 25, 35, and 45 kHz, respectively. The outputs of the modulators are combined prior to intensity modulation of the light Tx. An additive white Gaussian noise channel is considered. The Rx is the same as the Costas-loop architecture shown in Figure 3b. The demodulated output symbols are filtered using high order Bessel filters, which match the Tx filter to mitigate inter-band interference. The $f_{\text{quiescient}}$ of the VCO can be selected for the desired band. A parametric signal generated by an arbitrary waveform generator (AWG) is added to the input of the VCO to simulate frequency deviations between the Tx and the Rx. Simulated performance metrics include the demodulated symbols non-data aided error vector magnitude (EVM), loop lock time, and moving standard deviation $u_d(t)$. Note, non-data aided EVM does not considers errors in the demodulation since it measures the constellation dispersion relatively to the nearest constellation symbol. However, there is a relation between data aided and non-data aided EVM, which is also related to the signal-to-noise ratio [26]. We considered three scenarios to evaluate the system synchronisation capability.

1. **Pull-in range Δf_P:** Initially we have, $f_{\text{quiescient}} = f_c$, there is a waiting period for the system to be synchronised, and later, a changing u_f signal at the VCO input, which will cause unwanted f_{LO} changes. Since the system is of type-II, it should be able to maintain the locked state without any phase error when a change in frequency occurs. Measurements include the pull-in range T_P and the verification that the loop can maintain a locked state without any phase error. This simulation only considers one band (i.e. $f_c = 25$ kHz).

2. **Lock range Δf_L and lock time ΔT_L:** Initially we have set the frequency deviation $f_{\text{quiescient}} = f_c + f_{\text{err}}$, where f_{err} is the initial offset between the Tx and the Rx frequencies. The loop lock time T_L, and lock range Δf_L are measured by looking at the EVM and moving standard deviation which provide information of if and when the loop entered in the lock state. This simulation also considers one band (i.e. $f_c = 25$ kHz).

3. **Noise and inter-band interference:** We validated the loop performance under noise conditions and compared the EVM of the Rx constellation with the EVM of an ideally
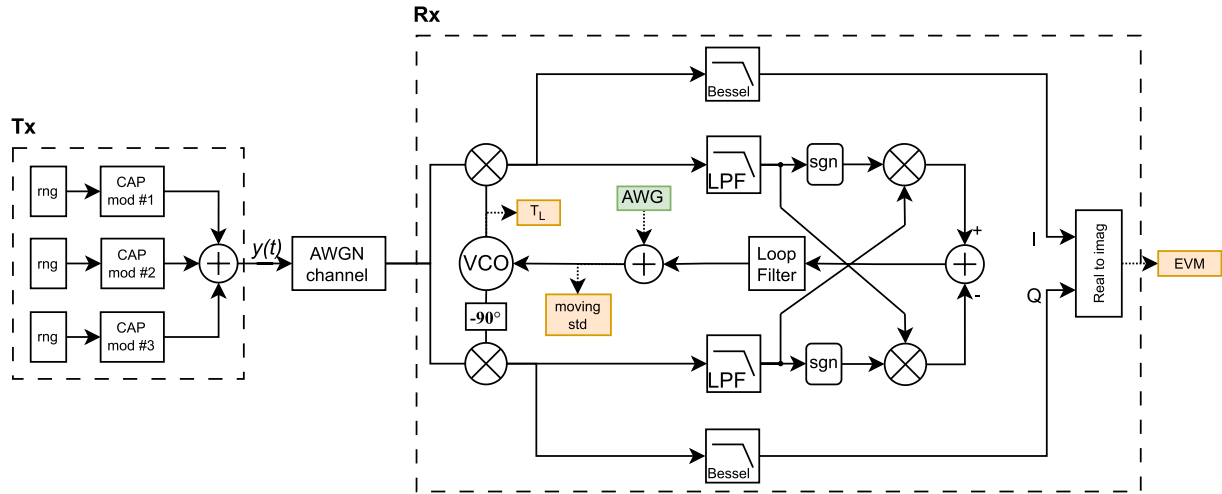
FIGURE 7 Simulation block diagram: in the Tx side, independent random number generators (rng) feed three CAP modulators with different bands. The combined signal is the sum of all Tx signals, forming the m-CAP signal $y(t)$. The AWGN channel model is used with variable noise variance. The Rx implements a Costas-loop, however with a different output for signal analysis with dedicated LPF. Measurements include the demodulated symbols EVM, the loop lock time, and the moving standard deviation of $u_d(t)$. AWGN, additive white Gaussian noise; EVM, error vector magnitude; LPF, low-pass filter; m-CAP, multiband carrierless amplitude and phase.

synchronised Rx. The performance was also measured when neighbour bands were active. Two scenarios, with and without guard bands were considered in the simulation.

3.1 | Costas-loop parameters

To achieve a stable loop and good characteristics, the Cost-loop parameters need to be properly calculated. The loop parameters to be computed are: ω_3, ω_{LP}, τ_1, and K_0, which are given by:

$$\omega_c \geqslant \omega_3 \geqslant R \tag{10}$$

$$\omega_{LP} = \omega_c F \tag{11}$$

$$K_0 = \frac{\omega_c^2 \tau_1}{K_d} \tag{12}$$

where F is a ratio between ω_{LP} and ω_c. Note that τ_1 can be arbitrarily chosen in order to compute K_0, or vice-versa. Considering the third band, with $f_c = 253$ kHz, and $\tau_1 = 20 \times 10^{-6}$, the remaining parameters are computed using Equations (10)–(12), and are listed in the Table 2. The F ratio was chosen to be 0.01 in order to provide a phase margin >45° for loop stability. From the system Bode plot, shown in Figure 8, the obtained phase margin is approximately 49°.

4 | RESULTS

Using the simulation setup previously presented, we carried out the followings:

TABLE 2 Costas-loop parameters used in simulation.

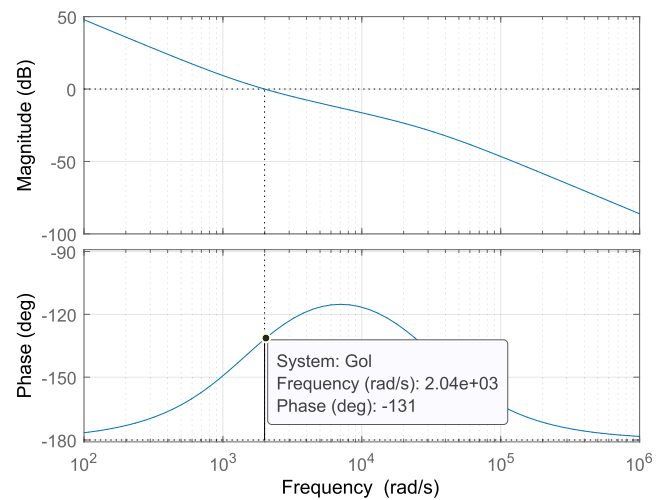| Parameter	Value
f_c	25 kHz
ω_c	1.5708×10^5 rad/s
F	0.01
ω_{LP}	1.5708×10^3 rad/s
ω_3	$2\pi R = 3.1416 \times 10^4$ rad/s
K_d	$2/\sqrt{2}$
τ_1	20×10^{-6} s
τ_2	6.3662×10^{-4} s
K_0	34.894

FIGURE 8 Designed Costas-loop transfer function open-loop Bode plot. The system phase margin is approximately 49°.

- Determining the pull-in range Δf_P for the system is in locked stated;
- Determining the lock range Δf_L and the lock time ΔT_L considering the initial frequency offset at the Rx;
- The loop performance considering noise and inter-band interference.

4.1 | Pull-in range Δf_P

Here, we consider two different conditions. (i), the frequency offset between the Tx and the Rx is set to zero, where the system is in the locked state. (ii), at 250 ms, a frequency step f_{step} is inserted at the Rx, where $f_{step} = \{10 + 25k \,|\, k \in \{1, 2, \ldots, 80\}\}$, using the AWG block in Figure 7. The moving standard deviation (MSTD) is measured at the input of the VCO and the results are shown in the Figure 9. Figure 9a shows the MSTD for each tested step sizes during the entire simulation time, and it is evident that the system is locked when MSTD presents low values, around 3.5. As depicted in Figure 9b, there are three possible outcomes after the frequency step at 250 ms: (i) the loop remains in its locked state (low MSTD), adjusting itself to the change in frequency; (ii) the system exits the locked state, but returns to the locked state after some time; and (iii) the system is unable to recover from a large f_{step}, and MSTD remains relativity high. In Figure 9c, the maximum measured MSTD after the frequency step is shown to assist in visualise where the loss of locked state occurs. Note, the MSTD reaches its saturated value of ≈ 24 beyond 800 Hz, indicating that this is the limit of the pull-in range. Therefore, $\Delta f_P \approx \pm 800$ Hz. Nevertheless, the results suggest that Δf_L may be slightly higher, since some of the simulated f_{step} values will regain lock state. From measuring the required time it takes for MSTD to begin converging to the lower value, we get ΔT_L of 3 ms. Based on the EVM of the Rx constellation shown in Figure 10, it is evident that the system is able to regain lock up to a f_{step} of 935 Hz, indicating that there is no static phase error relative to the reference constellation, which is a characteristic of type-II PLLs.

4.2 | Lock range Δf_L and lock time ΔT_L

Simulating the locked state acquisition requires setting the VCO frequency offset at the beginning of the simulation by changing $f_{quiescient}$. Initially, the system will not be in sync and the loop will attempt to lock. As the Tx introduces some latency into the signal, Rx will receive the signal after a deterministic period, defined by the average of the filter group delay $\overline{\tau_g} = 0.8055 \times 10^{-3}$s. A block T_L measures the loop's lock time by comparing its input frequency with its desired frequency value, within a tolerance. To simulate the purposes, the tolerance was set to 500 Hz, since based on the previous results the system is already locked at this frequency offset. By analysing Figure 11, the measured T_L has three main regions, depending on $\Delta f_c = f_c - f_{LO}$:
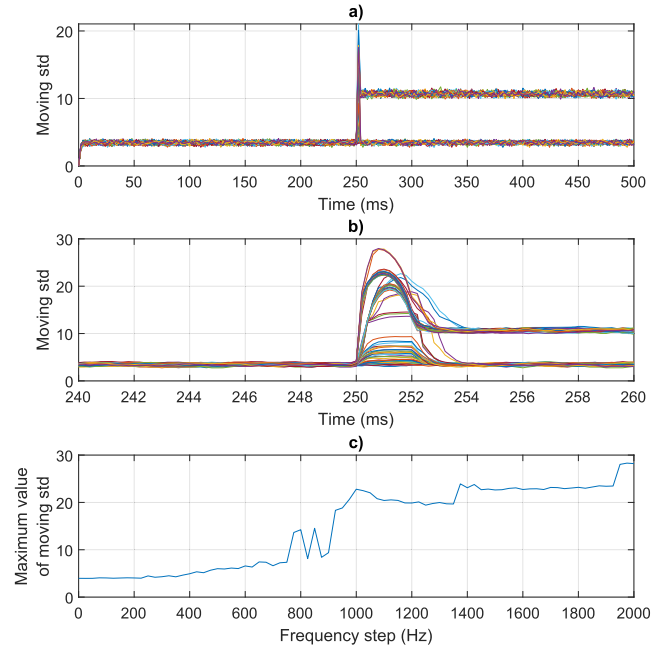

FIGURE 9 Pull-in simulation scenario where a frequency step with increasing amplitudes is inserted at 0.25 s: (a) moving standard deviation value of u_f, (b) moving standard deviation value of u_f in detail at 0.25 s; and (c) maximum value of moving standard deviation after the frequency step.
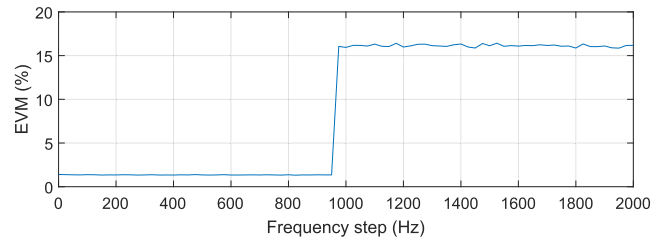

FIGURE 10 Final error vector magnitude (EVM) value of frequency step scenario.

- $|\Delta f_c| \geqslant 925$ Hz, the system cannot enter in the lock state. However, if this happens, the block measuring T_L will have a negative value of $-\overline{\tau_g}$;
- $550 \leqslant |\Delta f_c| \leqslant 900$ Hz, the system locks with a $T_L < 1.194 \times 10^{-3}$ s;
- $|\Delta f_c| \leqslant 525$ Hz, the system lock very fast with a $T_L = 194.4 \times 10^{-6}$ s.

From the T_L results, for $\Delta f_L \geqslant \pm 900$ Hz we can assume that the system should always lock after $T_L = 1.194 \times 10^{-3}$ s. Accordingly, and considering the symbol rate R from Table 1, the number of symbols required to send in the package preamble, for correct system lock, n_L, is determined as follows:

$$n_L = \lceil T_L R \rceil = \lceil 1.194 \times 10^{-3} \times 5 \times 10^3 \rceil = 6 \; symbols$$

$$(13)$$

Furthermore, since $\Delta f_L < \Delta f_{total}$, the loop can successfully lock and maintain its lock state. As depicted in Figure 11b the
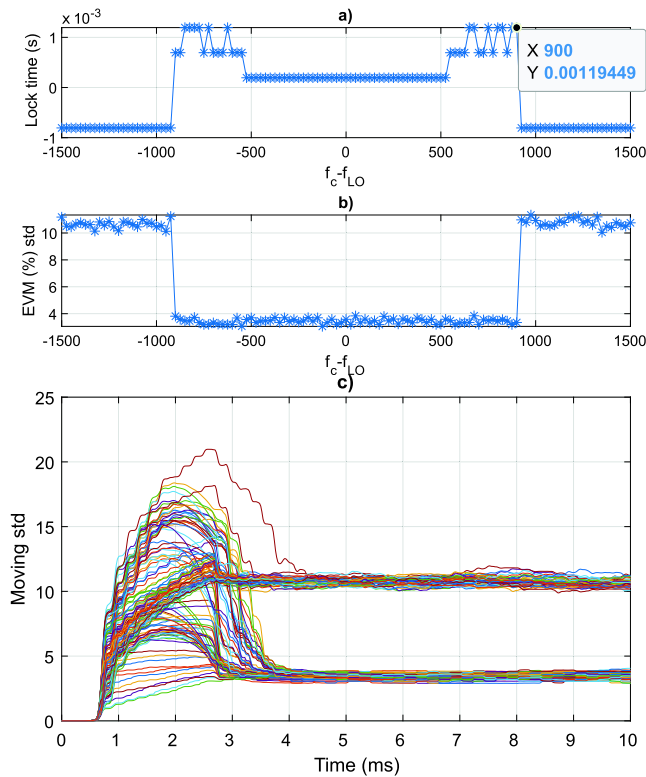
FIGURE 11 Simulation scenario where the Rx starts with a frequency offset $f_c - f_{LO}$: (a) measured lock time T_L, (b) measured EVM (%) on steady-state, (c) transient MSTD with observable $\overline{\tau_g}$. EVM, error vector magnitude; MSTD, moving standard deviation.

EVM in the steady-state is always fairly low when $\Delta f_c < \Delta f_L$, guaranteeing successfully demodulation. Finally, Figure 11c shows the MSTD, illustrating whether or not the system locks. Note, MSTD is about $\overline{\tau_g}$, waiting for the signal input and fully stabilising after about 3×10^{-3} s.

4.3 | Performance with noise and inter-band interference

As previously mentioned, the analysis was performed for the system with no noise and interference. However, in a real application, noise and interference from adjacent bands must be considered. We compared the average percentage RMS EVM of the demodulated constellation between the system, with and without Costas-loop, for three cases: (i) only channel noise; (ii) noise plus the odd bands (with guard bands); and (iii) noise plus all bands (without guard bands), as depicted in Figure 12. The correspondent EVM of the forward error correction limit was also included in the figure for easiness of interpretation. From the figure, The EVM follows the reference Rx quite accurately in both scenarios (i) and (ii), with a performance decrease of approximately 1 dB for E_b/N_0 between 2 and 8 dB. Note, for the first scenario, the measured EVM follows the curve for the QPSK non-data aided EVM presented in Ref. [26]. However the Costas-loop cannot accommodate the adjacent band interference in the third scenario. Note, there are no guard bands
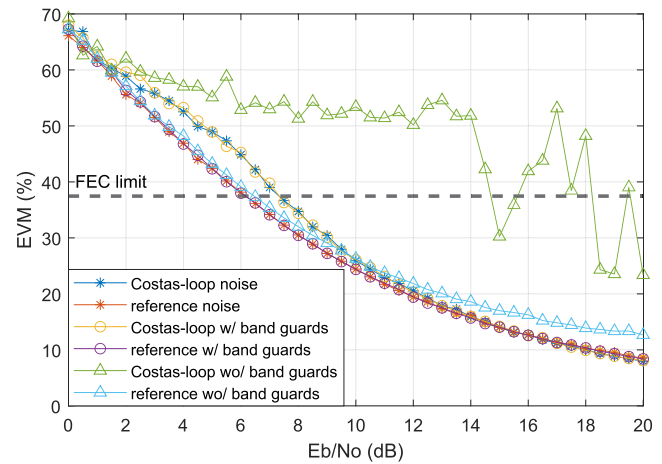

FIGURE 12 RMS EVM (%) versus E_b/N_0 (dB) for the reference Rx and the Costas-loop Rx for three scenarios: (i) only channel noise, (ii) noise + odd bands (with guard bands), and (iii) noise + all bands (without guard bands).

between the generated bands in this scenario. Possible solutions to improve the performance in such scenarios would be to increase the order of the LPF, alternatively, the use of a time-division multiple access (TDMA) scheme that utilises one set of bands, divided into even and odd bands, effectively resulting half of the system throughput in the second scenario.

5 | CONCLUSIONS

The results of this study demonstrated that an IoT multi-user communication system based on a central digital m-CAP Tx, broadcasting data on distinct channels, designed for multiple simple and low-cost/power devices, is technically viable. The minimal architecture these systems allow them to be mostly implemented in the analogue domain (with the advantageous of reduced energy consumption and cost), while still being able to decode the data. Specifically, this work addressed the particular problem of carrier synchronization, which is imperative in real implementations due to the imperfections of the devices and the delays in the system. We presented a Costas-loop simulation model, and obtained performance results, including pull-in and lock range, as well as the lock time. The results showed that the system was able to synchronise with a pull-in range of and lock ranges of $\approx \pm 800$ and $\approx \pm 900$ Hz, respectively. For the loop to be in the locked state within 1.194 ms, at least 6 data symbols must be sent prior to the data symbols in order to allow the system to synchronise for correct demodulation of the data symbols. Furthermore, $\Delta f_P < \Delta f_{total}$ allow the type-II filter to be used in the proposed architecture, which can be implemented using a reasonable circuit, potentially with low power consumption. Additionally, the performance of the system was determined when noise and interference from the other modulated bands were considered. This was achieved by measuring the EVM average and comparing it with an Rx that is perfectly synchronised with the incoming signal. The results showed that noise and interference from non-adjacent bands did

not degrade the performance of the system. However, the system was unable to lock due to interference from the adjacent bands. Higher PLL order, or TDMA schemes that alternately use even and odd bands are possible solutions to mitigate interference from adjacent bands, at the cost of a small increase in the complexity and cost of devices.

AUTHOR CONTRIBUTIONS

Luís Rodrigues: Conceptualization; Investigation; Methodology; Writing – original draft. **Mónica Figueiredo**: Conceptualization; Methodology; Supervision; Writing – review & editing. **Luís Nero Alves**: Conceptualization; Methodology; Supervision; Writing – review & editing. **Zabih Ghassemlooy**: Conceptualization; Methodology; Writing – review & editing.

ACKNOWLEDGEMENTS

CONFLICT OF INTEREST STATEMENT

The authors declare no conflicts of interest.

DATA AVAILABILITY STATEMENT

The data that support the findings of this study are available from the corresponding author upon reasonable request.

ORCID

Luís Rodrigues https://orcid.org/0000-0003-2593-3619
Mónica Figueiredo https://orcid.org/0000-0002-0780-3725

REFERENCES

1. Ding, J., et al.: IoT connectivity technologies and applications: a survey. IEEE Access 8, 67646–67673 (2020). https://doi.org/10.1109/access.2020.2985932
2. Yarali, A.: The Internet of Things (IoT), ch. 3, pp. 41–66. John Wiley & Sons, Ltd (2021). https://doi.org/10.1002/9781119685265.ch3
3. Cisco: Cisco Annual Internet Report (2018–2023), tech. rep. Cisco Systems, Inc (2020). https://www.cisco.com/c/en/us/solutions/collateral/executive-perspectives/annual-internet-report/white-paper-c11-741490.pdf
4. Akyildiz, I., et al.: A survey on sensor networks. IEEE Commun. Mag. 40(8), 102–114 (2002). https://doi.org/10.1109/mcom.2002.1024422
5. Portilla, J., et al.: The extreme edge at the bottom of the Internet of Things: a review. IEEE Sensor. J. 19(9), 3179–3190 (2019). https://doi.org/10.1109/jsen.2019.2891911
6. Laughlin, L., et al.: Emerging hardware enablers for more efficient use of the spectrum. In: 2019 IEEE International Symposium on Dynamic Spectrum Access Networks (DySPAN), pp. 1–9 (2019)
7. Vondrouš, O., et al.: Performance evaluation of IoT mesh networking technology in ism frequency band. In: 2016 17th International Conference on Mechatronics - Mechatronika (ME), pp. 1–8 (2016)
8. Figueiredo, M., Alves, L.N., Ribeiro, C.: Lighting the wireless world: the promise and challenges of visible light communication. IEEE Consum. Electron. Mag. 6(4), 28–37 (2017). https://doi.org/10.1109/mce.2017.2714721
9. T. F. H. H. Institute: First real-time test of Li-Fi utilization for the industrial internet of things. 6 (2018)
10. Fernández-Caramés, T.M., Fraga-Lamas, P.: A review on human-centered IoT-connected smart labels for the industry 4.0. IEEE Access 6, 25939–25957 (2018). https://doi.org/10.1109/access.2018.2833501
11. Barraca, J.P., Alves, L.N., Figueiredo, M.: Electronic shelf labeling employing visible light communication concepts. In: 2014 9th International Symposium on Communication Systems, Networks Digital Sign (CSNDSP), pp. 1017–1022 (2014)
12. Perković, T., Kovačević, T., Čagalj, M.: Blinkcomm: initialization of IoT devices using visible light communication. Wireless Commun. Mobile Comput. 2018, 8523078–16 (2018). https://doi.org/10.1155/2018/8523078
13. Teramoto, S., Ohtsuki, T.: Optical wireless sensor network system using corner cube retroreflectors (CCRs). In: IEEE Global Telecommunications Conference, 2004, vol. 2, pp. 1035–1039. GLOBECOM '04 (2004)
14. Khourn, K., et al.: Performance evaluation of optical wireless identification scheme employing thinfilm corner cube retroreflector. In: 2013 IEEE 24th Annual International Symposium on Personal, Indoor, and Mobile Radio Communications (PIMRC), pp. 3599–3604 (2013)
15. Li, J., et al.: Retro-VLC: enabling battery-free duplex visible light communication for mobile and IoT applications. In: Proceedings of the 16th International Workshop on Mobile Computing Systems and Applications, HotMobile '15, pp. 21–26. Association for Computing Machinery, New York (2015)
16. Yun, J., Jang, B.-J.: Ambient light backscatter communication for IoT applications. J. Electromagn. Eng. Sci. 16(4), 214–218 (2016). https://doi.org/10.5515/jkiees.2016.16.4.214
17. Shao, S., Khreishah, A., Elgala, H.: Pixelated VLC-backscattering for self-charging indoor IoT devices. IEEE Photon. Technol. Lett. 29(2), 177–180 (2017). https://doi.org/10.1109/lpt.2016.2631946
18. Mohammedi Merah, M., Guan, H., Chassagne, L.: Experimental multi-user visible light communication attocell using multiband carrierless amplitude and phase modulation. IEEE Access 7, 12742–12754 (2019). https://doi.org/10.1109/access.2019.2893451
19. Rodrigues, L., Figueiredo, M., Alves, L.N.: Analog m-CAP demodulation for VLC-based IoT systems. In: 2020 12th International Symposium on Communication Systems, Networks and Digital Signal Processing (CSNDSP), pp. 1–6 (2020)
20. Rodrigues, L., et al.: Experimental validation of analog m-CAP receivers for Internet of Things. In: 2022 13th International Symposium on Communication Systems, Networks and Digital Signal Processing (CSNDSP), pp. 26–31 (2022)
21. Sklar, B.: Digital Communications: Fundamentals and Applications. Prentice-Hall, Inc., Upper Saddle River (1988)
22. Rodrigues, L., Figueiredo, M., Alves, L.N.: Optimized analog multi-band carrierless amplitude and phase modulation for visible light communication-based internet of things systems. Sensors 21(7), 2537 (2021). https://doi.org/10.3390/s21072537
23. Rodrigues, L., et al.: VLC frontends for IoT applications. In: 2022 4th West Asian Symposium on Optical and Millimeter-Wave Wireless Communications (WASOWC), pp. 1–6 (2022)
24. Products, M.I.: Using a VCXO (Voltage-Controlled Crystal Oscillator) as a Clock (CLK) Generator. tech. rep. Analog Devices, Inc. (2004)
25. Best, R.: Costas Loops: Theory, Design, and Simulation. Springer International Publishing (2018)
26. Mahmoud, H.A., Arslan, H.: Error vector magnitude to SNR conversion for nondata-aided receivers. IEEE Trans. Wireless Commun. 8(5), 2694–2704 (2009). https://doi.org/10.1109/twc.2009.080862